Journal of Aerosol Science 105 (2017) 108–127

Contents lists available at ScienceDirect

Journal of Aerosol Science

journal homepage: www.elsevier.com/locate/jaerosci

# Numerical investigation of the interaction, transport and deposition of multicomponent droplets in a simple mouth-throat model

Xiaole Chen[a], Yu Feng[b], Wenqi Zhong[a,*], Clement Kleinstreuer[c]

[a] Key Laboratory of Energy Thermal Conversion and Control of Ministry of Education, Southeast University, Nanjing, Jiangsu Prov. 210096, China
[b] School of Chemical Engineering, Oklahoma State University, Stillwater, OK 74078, USA
[c] Joint UNC-NCSU Department of Biomedical Engineering, North Carolina State University, Raleigh, NC 27695, USA

ARTICLE INFO

*Keywords:*
**Multicomponent droplet inhalation**
**droplet-vapor interaction**
**airway-wall condition**
**hygroscopic growth**
**deposition efficiency**

ABSTRACT

A basic analysis of inhaled multicomponent droplet-vapor interaction and subsequent aerosol deposition is very important for the understanding of natural phenomena as well as for health-care related applications. Employing a highly idealized mouth-throat (MT) model as a test bed, the transport and deposition mechanisms of a water-droplet are simulated, considering ethanol, sodium chloride and fluorescein as components. The flow-field equations are solved with a validated transition SST model which can predict the effects of flow rate, relative humidity (RH), and wet *vs.* dry airway walls on aerosol deposition efficiency (DE). The simulation results indicate that the hygroscopic growth of sodium chloride particles is sensitive to the saturation pressure of water vapor. A high flow rate decreases the RH in the airways as well as the average growth ratios of deposited and escaped droplets; but, still increases the DE. When compared to a dry boundary condition, the wet airway-wall increases the DE up to 4.6% when RH = 30% and the flow rate is 60 L/min. It also increases the average growth ratio of deposited droplets notably, i.e., larger than 0.5 for most conditions, while its effect on the average growth ratio of deposited droplets is not apparent. A high inlet RH can significantly enhance the hygroscopic growth of the droplets and DE, especially when it is larger than the RH threshold for the hygroscopic component. Besides, it can elevate the growth ratios of deposited and escaped droplets at the same time, which could be utilized to reduce the deposition of submicron hygroscopic aerosol in the upper airway.

## 1. Introduction

From air pollutants to cigarette smoke particles and pharmaceutical aerosols, many inhalable aerosols contain soluble and/or volatile components. As the humidity conditions in the human airways are normally higher than in the ambient atmosphere, these components can interact with water vapor, causing a change in aerosol size. Thus, aerosol - vapor interactions can significantly influence the trajectories of the aerosols and hence lung deposition.

Numerous experiments and simulations have been carried out to investigate the mechanisms of such aerosol - vapor interactions and to improve the efficiency of inhalers. For example, Cheng, Kleinstreuer, Kim and Zhang (2004a) numerically analyzed the effect of evaporation on JP-8 fuel droplet deposition in a human upper airway model. Later on, Kleinstreuer, Kim and Zhang (2006a) studied evaporative and hygroscopic effects on saline droplet deposition in upper airways, and concluded an increase in solute

* Corresponding author.

http://dx.doi.org/10.1016/j.jaerosci.2016.12.001
Received 20 April 2016; Received in revised form 27 October 2016; Accepted 12 December 2016
Available online 22 December 2016

## Nomenclature

| | |
|---|---|
| $A$ | surface area of the droplet |
| $a_1$, $a_2$, $a_3$ | constants determined by particle Reynolds number |
| $\alpha_m$ | mass thermal accommodation coefficient |
| $C_1$,$C_2$ | constants in Eq. (31). |
| $C_c$ | Cunningham correction factor |
| $C_D$ | drag coefficient |
| $C_{Dd}$ | drag force coefficient for droplet |
| $Cd_\omega$ | cross-diffusion term |
| $C_m$ | Fuchs-Knudsen number correction |
| $C_\mu$ | coefficient in the turbulent model |
| $c_{d,i}$ | specific heat of the component $i$ in the droplet |
| $D$ | inlet diameter |
| $D_e$ | mass diffusivity of component $e$ |
| $D_w$ | mass diffusion coefficient for water vapor |
| $\overline{D}_k$ | modified term of destruction of turbulence kinetic energy |
| $D_\omega$ | dissipation of $\omega$ |
| $d_d$ | droplet diameter |
| $E_{\gamma 1}$, $E_{\gamma 2}$ | transition source and destruction source terms |
| $f_i$ | damping functions for fluctuating velocity in near-wall region, $i = u, v, w$ |
| $f_u$ | streamwise damping function |
| $f_v$ | damping function normal to the nearest wall |
| $f_w$ | damping function normal to $f_u$ and $f_v$ |
| $G_i$ | zero-mean, unit variance independent Gaussian random numbers |
| $\vec{g}$ | gravitational acceleration |
| $i$ | van't Hoff factor |
| $K_e$ | Kelvin effect correction for component $e$ |
| $K_w$ | Kelvin effect correction for water vapor |
| $Kn$ | Knudsen number |
| $k$ | turbulence kinetic energy |
| $l_e$ | eddy length scale |
| $L_e$ | latent heat of evaporable component $e$ |
| $M_e$ | molar mass of the component of interest $e$ |
| $m_d$ | mass of the droplet |
| $m_{d,i}$ | mass of the component $i$ in the droplet |
| $\overline{n}_e$ | the average mass flux of evaporable component $e$ on the droplet surface |
| $n_e$ | mass flux of evaporable component $e$ |
| $Nu$ | Nusselt number of the droplet |
| Pr | Prandtl number |
| $P_k$ | production of turbulence kinetic energy |
| $\widetilde{P}_k$ | modified term of $P_k$ with intermittency |
| $P_{ve,sat}(T_d)$ | saturation pressure of component $e$ under temperature $T_d$ |
| $P_{\gamma 1}$, $P_{\gamma 2}$ | transition source and destruction source terms |
| $P_{\theta t}$ | source term in Eq. (5). |
| $p$ | fluid pressure |
| $R$ | universal gas constant |
| $R_e$ | gas constant of component $e$ |
| $R_w$ | gas constant of water vapor |
| $r_\infty$ | radius of the air around the droplet |
| $\mathrm{Re}_d$ | droplet Reynolds number |
| $\mathrm{Re}_{\theta t}$ | critical Reynolds number |
| $R\tilde{e}_{\theta t}$ | transport scalar for momentum thickness Reynolds number |
| RH | relative humidity |
| $Sc$ | Schmidt number |
| $Sc_t$ | turbulent Schmidt number |
| $Sh$ | Sherwood number of the droplet |
| $T_a$ | temperature of the surrounding air |
| $T_d$ | droplet temperature |
| $T_L$ | fluid Lagrangian integral time |
| $t$ | time |
| $t_{cross}$ | eddy crossing time |
| $t_1$, $t_2$, $t_3$ | constants in Eq. (30). |
| $u$ | fluid velocity |
| $\vec{u}_d$ | velocity vector of the droplet |
| $u_i$ | instantaneous velocity of the fluid, $i=x, y, z$ |
| $\overline{u}_i$ | time average velocity |
| $u_i'$ | fluctuating component |
| $x_e$ | mole fraction of $e$ in the droplet |
| $x_s$ | mole fraction of soluble component, i.e., NaCl in the validation case |
| $x_w$ | mole fraction of water |
| $Y_{e,surf}$ | mass fraction of the evaporable component $e$ on the interface of the droplet |
| $Y_{e,\infty}$ | mass fraction of the evaporable component $e$ in the surrounding gas |
| $Y_w$ | mass fraction of the water vapor |
| $Y_{w,surf}$ | mass fraction of the water vapor on the interface of the droplet |
| $Y_{w,\infty}$ | mass fraction of the water vapor in the surrounding air |
| $y$ | distance to the nearest wall |
| $y^+$ | dimensionless wall distance |

### Greek

| | |
|---|---|
| $\alpha_m$ | mass thermal accommodation coefficient |
| $\Delta T$ | temperature change in one time step |
| $\gamma$ | intermittency |
| $\gamma_e$ | activity coefficient of component $e$ |
| $\gamma_w$ | water activity coefficient |
| $\xi_i$ | random numbers from standard normal distribution |
| $\lambda$ | gas mean free path |
| $\lambda_g$ | thermal conductivity of the surrounding gas |
| $\mu$ | dynamic viscosity of the fluid |
| $\mu_t$ | turbulent viscosity |
| $\upsilon$ | kinematic viscosity of the fluid |
| $\upsilon_t$ | turbulent eddy viscosity |
| ρ | fluid density |
| $\rho_d$ | droplet density |
| $\rho_g$ | density of surrounding gas |
| $\rho_{vw,sat}$ | saturation water vapor density |
| $\sigma$ | surface tension of the droplet |
| $\sigma_k$ | turbulent Prandtl number for $k$ |
| $\sigma_\omega$ | turbulent Prandtl number for $\omega$ |
| $\tau$ | particle relaxation time |
| $\tau_e$ | eddy lifetime |
| $\tau_w$ | wall shear stress |
| $\phi$ | heat flux |
| $\omega$ | specific dissipation rate |

*Subscripts*

| | | | |
|---|---|---|---|
| *a* | air | *m* | mass |
| *D* | drag force | *s* | soluble component in the droplet |
| *d* | droplet | *u* | velocity component in x direction |
| *e* | evaporable component in the droplet / eddy | *v* | velocity component in y direction |
| *i* | component in droplet / velocity components / directions in Cartesian coordinates | *w* | velocity component in z direction / water / water vapor |
| | | *k* | turbulent kinetic energy |
| | | *ω* | specific dissipation rate |

concentration and inlet relative humidity, or a decrease of inlet air temperature can enhance the deposition of sodium chloride (NaCl) droplets. Furthermore, Kim, Kleinstreuer and Zhang (2006b) investigated the water vapor transport and its effect on the hygroscopic droplet deposition. The results indicated that vaporization has a significant influence on the deposition of isotonic saline droplets in mouth-throat and G0-G3 airways. Longest and Xi (2008) concluded that the condensational growth may enhance the deposition of cigarette smoke particles in airways. Hindle, Longest and McLeskey (2010) further proposed the concept of enhanced condensational growth (ECG), which uses the condensational growth to increase the delivery efficiency of submicron aerosols into deeper lung regions. Finlay and Javaheri (2013) proved that two methods, i.e., heating the aerosol stream and adding dry NaCl particles into the aerosol steam, can reduce extra-thoracic deposition. The goal of these approaches is to control the RH distribution in the upper lung airways and subsequently reduce, via hygroscopic growth, early drug-aerosol deposition.

Kim, Si, Xi and Zhou (2013) reported that a 400 nm NaCl droplet can reach its equilibrium diameter within less than 0.1 ms for evaporation or hygroscopic growth condition. Thus, the evaporation and growth of the aerosol is a rapid progress when compared to the whole process of aerosol transport in the airway. Meanwhile, there is a threshold humidity that deliquescent salt aerosol start to grow, e.g., 75% for NaCl aerosol (Cruz & Pandis, 2000; Nenes, Pandis & Pilinis, 1998; Tang, Munkelwitz & Davis, 1977). This suggests that the hygroscopic growth of the aerosol relates to the local RH distribution, especially in the near-wall regions. However, due to limitations of current manufacturing methods, e.g., 3D printing and stereolithography, it is still difficult to reproduce the characteristics of mucus covered airways, which can constantly humidify the incoming air. Thus, it is of interest to investigate the effects of flow rate, degree of airway-wall wetness and inlet RH on the RH distribution in the airways and their subsequent effects on hygroscopic aerosol transport and deposition via numerical methods.

The objective of the present study is to predict numerically the transport and deposition of multicomponent droplets in a highly idealized mouth-throat (MT) airway with a validated aerosol-vapor interaction and laminar-turbulent transport model, considering different inlet and boundary conditions. Specifically, the effects of flow rate, wet *vs.* dry airway walls and inlet humidity are analyzed on the distribution of RH in the MT model as well as the transport and deposition of hygroscopic droplets, including deposition efficiency (DE), spatial and size distributions of deposited/escaped droplets and the final growth ratios of the droplets. The new results indicate that hygroscopic growth of the deliquescent aerosols, i.e., NaCl in this study, closely relates to the local RH-level in the airways, especially in the boundary regions with high RH gradients. It was also found that large RH-values can elevate the growth ratios of deposited and escaped droplets. In turn, that could be utilized to reduce the deposition caused by nanoparticles subject to Brownian motion effects. Considering the high sensitivity of the hygroscopic growth of the NaCl – water droplet to the ambient temperature and RH conditions, future work will focus on applications of the fundamental results to subject-specific airway configurations, including the heat transfer between the airway tissue, mucus layer and airflow.

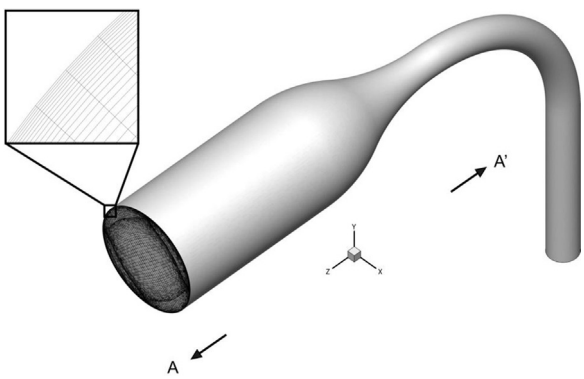


**Fig. 1.** Mouth-throat airway geometry and mesh.

## 2. Method

### 2.1. Geometry

Finlay, Matida and Zhang (2004b) proposed a highly idealized MT model, and suggested that it was a better candidate for pharmaceutical standard than USP throats. Chia, Finlay and Zhang (2006c) continued to analyze the effect of the outlet diameter of the model on DE. The results indicated that models with outlet diameters of 7.5 and 8.5 mm were better in accordance to in vivo experimental data. In this paper, the highly idealized MT model (Zhang et al. 2004b) with an outlet diameter of 8.5mm was selected as the test bed to evaluate the hygroscopic droplet transport and deposition in the mouth-throat airway. The inlet diameter of the MT model was 30 mm.

A hexahedral mesh was generated for the computational analysis. The mesh independence was tested. The finial mesh number was 2, 752, 512, and the $y^+$ of the first layer meshes were ensured smaller than 1 based on the requirement of the transition SST model. $y^+$ is a dimensionless wall distance defined as

$$y^+ = \frac{y}{\upsilon}\sqrt{\frac{\tau_w}{\rho}} \tag{1}$$

where $y$ is the distance to the nearest wall, $\tau_w$ is the wall shear stress. The MT model geometry and mesh structure are shown in Fig. 1. The positive and negative z directions are referred as A and A' directions as plotted in Fig. 1 in the following sections.

### 2.2. Governing equations for fluid

Transition from laminar to turbulent flow would occur near the contracting mouth cavity at 15 to 45 L/min conditions (see Table 1). Thus, this requires the numerical prediction to accurately capture the transition phenomenon. The transition SST turbulence model has been proved to be not only a better method for transitional flow than conventional RANS approach (Menter, Langtry & Völker, 2006a), but also suitable for gas-solid flow in airway researches (Kleinstreuer & Zhang 2011).

The transition SST model was applied to solve the laminar-turbulent transitional and turbulent flow. The governing equations for the fluid phase are (Menter et al. 2006a, 2006b):

$$\frac{\partial}{\partial t}(\rho k) + \frac{\partial}{\partial x_j}(\rho u_j k) = \widetilde{P}_k - \widetilde{D}_k + \frac{\partial}{\partial x_j}\left(\left(\mu + \frac{\mu_t}{\sigma_k}\right)\frac{\partial k}{\partial x_j}\right) \tag{2}$$

$$\frac{\partial}{\partial t}(\rho\omega) + \frac{\partial}{\partial x_j}(\rho u_j \omega) = \alpha\frac{P_k}{\upsilon_t} - D_\omega + Cd_\omega + \frac{\partial}{\partial x_j}\left(\left(\mu + \frac{\mu_t}{\sigma_\omega}\right)\frac{\partial \omega}{\partial x_j}\right) \tag{3}$$

where $\widetilde{P}_k$ and $\widetilde{D}_k$ are the modified production and destruction terms of turbulence kinetic energy based on the original SST turbulence model, using intermittency coefficient $\gamma$. The intermittency $\gamma$ can be solved by

$$\frac{\partial(\rho\gamma)}{\partial t} + \frac{\partial(\rho u_j \gamma)}{\partial x_j} = P_{\gamma 1} - E_{\gamma 1} + P_{\gamma 2} - E_{\gamma 2} + \frac{\partial}{\partial x_j}\left(\left(\mu + \frac{\mu_t}{\sigma_f}\right)\frac{\partial \gamma}{\partial x_j}\right) \tag{4}$$

Since the critical Reynolds number $\mathrm{Re}_{\theta c}$ is required for calculating the transition source term $P_{\gamma 1}$, a transported scalar $R\tilde{e}_{\theta t}$ is used in the transport equation below to calculate $\mathrm{Re}_{\theta c}$

$$\frac{\partial(\rho R\tilde{e}_{\theta t})}{\partial t} + \frac{\partial(\rho u_j R\tilde{e}_{\theta t})}{\partial x_j} = P_{\theta t} + \frac{\partial}{\partial x_j}\left(\sigma_{\theta t}(\mu + \mu_t)\frac{\partial R\tilde{e}_{\theta t}}{\partial x_j}\right) \tag{5}$$

The details of transition SST model and correction for separation induced transition are documented in literature (Menter et al. 2006a, 2006b).

The transport equation for the water vapor is controlled by (Bird, Lightfoot & Stewart 1960):

**Table 1**
Inlet and outlet flow parameters.

| Parameters | Values | | | |
|---|---|---|---|---|
| Air density (37°C) [kg/m$^3$] | 1.135 | | | |
| Air dynamic viscosity (37°C) [kg/m·s] | $2.00\times10^{-5}$ | | | |
| Inlet diameter [m] | 0.03 | | | |
| Outlet diameter [m] | 0.085 | | | |
| Flow rate [L/min] | 15 | 30 | 45 | 60 |
| Inlet Reynolds number | 697 | 1 395 | 2 093 | 2 791 |
| Outlet Reynolds number | 2 463 | 4 926 | 7 389 | 9 852 |

$$\frac{\partial \rho Y_w}{\partial t} + \frac{\partial \rho u_j Y_w}{\partial x_j} = \frac{\partial}{\partial x_j}\left[\left(\rho D_w + \frac{\mu_t}{Sc_t}\right)\left(\frac{\partial Y_w}{\partial x_j}\right)\right] \tag{6}$$

where $Y_w$ is the mass fraction of water vapor, $D_w$ is the mass diffusion coefficient for water vapor and $Sc_t$ is the turbulent Schmidt number.

### 2.3. Governing equations for particle and droplet

#### 2.3.1. Particle and droplet transport

In light of the large aerosol-to-air density ratio, negligible aerosol rotation and limited thermophoresis, the trajectories of the particles or droplets could be determined based on the sphere particle assumption:

$$m_d \frac{d\vec{u}_d}{dt} = \frac{1}{8}\pi \rho d_d^2 C_{Dd}(\vec{u} - \vec{u}_d)|\vec{u} - \vec{u}_d| + m_d \vec{g} \tag{7}$$

where $d_d$ is the droplet diameter, and the drag force coefficient $C_{Dd}$ is defined by

$$C_{Dd} = C_D/C_c \tag{8}$$

where $C_c$ is the Cunningham correction factor (Allen & Raabe, 1985) and the drag coefficient $C_D$ is defined by (Morsi & Alexander, 1972)

$$C_D = a_1 + \frac{a_2}{\mathrm{Re}_p} + \frac{a_3}{\mathrm{Re}_p^2} \tag{9}$$

where the constants $a_1$, $a_2$ and $a_3$ are determined by the particle Reynolds number.

For turbulent flow, the instantaneous fluid velocity $u$ comprises two components

$$u_i = \bar{u}_i + u_i' \quad i = x, y, z \tag{10}$$

where $\bar{u}_i$ is the average velocity over time, and $u_i'$ is the fluctuating component representing the randomly directed eddy. For the isotropic region, the fluctuating component $u_i'$ can be calculated by (Gosman & Loannides, 1983)

$$u_i' = \xi_i \sqrt{\frac{2}{3}k} \tag{11}$$

where $\xi_i$ are the random numbers from standard normal distribution. However, the DNS results indicated that the fluid in the near-wall region is anisotropic, and that the fluctuating velocity of the fluid can be modeled by applying damping functions in different directions (Kim, Moin & Moser, 1987; Wang & James, 1999), i.e.

$$u_i' = f_i \xi_i \sqrt{\frac{2}{3}k} \tag{12}$$

$$f_u = 1 + 0.285(y^+ + 6)exp[-0.455(y^+ + 6)^{0.53}] \tag{13}$$

$$f_v = 1 - \exp(-0.02y^+) \tag{14}$$

$$f_w = \sqrt{3 - f_u^2 - f_v^2} \tag{15}$$

where $f_u$ is the function for stream-wise direction, $f_v$ is normal to the closest wall, and $f_w$ is vertical to $f_u$ and $f_v$. Eqs. (13)–(15) were applied for areas where the $y^+$ values were less than 80.

Even though these functions are derived from a duct flow, they are reasonably accurate for a wider range of geometries (Wang & James, 1999). Finlay, Grgic, Lange and Matida (2004) applied this near-wall correction (NWC) for the aerosol deposition in an idealized mouth-throat model, and suggested that simulation with the anisotropic correction fitted the experiment better. This method is also utilized for the tracking of cigarette smoke particles (Longest & Xi, 2008; Hyun, Kleinstreuer & Zhang 2012). Abouali, Ahmadi, Emdad and Ghahramani (2014) adopted similar approach using particle Stokes number instead of $y^+$ as the variable to determine the particle trajectory in the laminar sublayer.

As the region of $y^+ < 80$ covers several layers of the mesh from the surface, a search function was implemented for the meshes not located on the boundary surface by user-defined function (UDF). For a given not-near-wall cell, say Cell A, the function loops through the cells on the surface to find the specific cell, say Cell S, which contains the surface mesh element that is closest to the Cell A. Thus, the distance to the nearest wall can be determined for Cell A, and the $y^+$ value for Cell A can be calculated via Eq. (1) by obtaining the wall shear stress in Cell S. $y^+$ values for all cells can be obtained by repeating this method in a loop. Finally, the damping function for the fluctuating velocity can be applied if the $y^+$ is smaller than 80.

The eddy interaction model (EIM), or known as random walk model (Matida et al., 2004), was applied to simulate the effect of the eddy on particle motion. It is assumed that a new particle-eddy interaction begins when the particle crosses the eddy $t_{cross}$ or the eddy lifetime $\tau_e$ ends depending on which is smaller. The two characteristic time variables can be defined as (Fluent 14.5 users guide, 2012; Gosman & Loannides, 1983)

$$\tau_e = -T_L \ln(r) \tag{16}$$

where $r$ is a uniform random number ranging from 0 to 1, and $T_L$, the fluid Lagrangian integral time can be approximated by

$$T_L \approx \frac{0.15}{\omega} \tag{17}$$

The particle eddy crossing time $t_{cross}$ is defined as

$$t_{cross} = -\tau \ln\left[1 - \frac{l_e}{\tau|u - u_p|}\right] \tag{18}$$

where $l_e$ is the eddy length scale defined as

$$l_e = (C_\mu)^{3/4}\frac{k^{1/2}}{\omega} \tag{19}$$

*2.3.2. Multicomponent droplet – vapor interactions*

In general, to construct a universal aerosol condensation / evaporation model as well as coding a proper program, the components in the droplet (or particle) are grouped into categories and reasonable assumptions have been made to reduce complexity:

1. Soluble and evaporable components
   The evaporable components directly lead to droplet-size change due to the mass transfer through the liquid-gas interface.
2. Soluble but non-evaporable components
   The soluble but non-evaporable components normally do not experience mass change during the aerosol growth / evaporation process. However, they occupy certain parts of the surface area at the liquid-gas interface. Thus, they reduce the mass fractions of the evaporable components on the droplet side, and hence affect the droplet diameter at the equilibrium state.
3. Insoluble and non-evaporable components.

The insoluble and non-evaporable components have a limited effect on particle growth / evaporation, except their contributions to the aerosol size and thermal capacity.

The change in droplet (or particle) mass can be derived from the mass change of each evaporable component (Longest & Kleinstreuer, 2005; Zhang et al., 2012; Feng, Castro, Kleinstreuer & Rostami, 2016):

$$\frac{dm_d}{dt} = -\sum_{e=1}^{k}\int_{surf} n_e dA \approx -\sum_{e=1}^{k}(\bar{n}_e \cdot A) \tag{20}$$

where $\bar{n}_e$ is the average mass flux of evaporable component $e$ on the surface. It can be expressed as:

$$\bar{n}_e = \frac{\rho_g Sh \bar{D}_e C_m}{d_d} \ln\frac{1 - Y_{e,\infty}}{1 - Y_{e,surf}} \tag{21}$$

where $\rho_g$ is the density of the surrounding gas; $Sh$ is the Sherwood number (Clift, Grace & Weber, 1978), defined as

$$Sh = \sqrt[3]{1 + \mathrm{Re}_d \cdot Sc} \cdot \max\left[1, Re_d^{0.077}\right] \tag{22}$$

where $Sc$ is the Schmidt number, defined as $Sc = \frac{\mu}{\rho D_e}$, and $D_e$ is the mass diffusivity of component $e$.

In Eq. (21), $Y_{e,surf}$ and $Y_{e,\infty}$ are the mass fractions of evaporable component $e$ on the droplet surface and in the gas phase far from the droplet, respectively; $C_\mathrm{m}$ is known as the Fuchs-Knudsen number correction (Ferron, Kreyling & Haider, 1988), defined as:

$$C_m = \frac{1 + Kn}{1 + (\frac{4}{3\alpha_m} + 0.377)Kn + \frac{4}{3\alpha_m}Kn^2} \tag{23}$$

where $Kn$ is the Knudsen number, $Kn = 2\lambda/d_d$, $\lambda$ is the gas mean free path, and $\alpha_m$ is the mass thermal accommodation coefficient (Fuchs & Sutugin, 1969).

The mass fraction of component $e$ on the surface $Y_{e,surf}$ can be obtained from the modified Raoult's law (Finlay, 2001; Longest & Xi, 2008; Zhang et al., 2012; Feng et al. 2016):

$$Y_{e,surf} = \gamma_e x_e K_e \frac{P_{ve,sat}(T_d)}{\rho R_e T_d} \tag{24}$$

where $\gamma_e$ is the activity coefficient of component $e$, $x_e$ is the mole fraction of $e$ in the droplet, $R_e$ is gas constant, $T_d$ is the droplet temperature, $P_{ve,sat}(T_d)$ is the saturation pressure of component $e$ at temperature $T_d$, and $K_e$ is the correction for Kelvin effect, which considers the higher vapor concentration at highly curved surfaces when compared to a flat surface (Finlay, 2001). $K_e$ is defined as

$$K_e = e^{\frac{4\sigma M_e}{R\rho_d d_d T_d}} \tag{25}$$

where $\sigma$ is the surface tension of the droplet, $M_e$ is the molar mass of the component $e$, $R$ is the universal gas constant, and $\rho_d$ is the

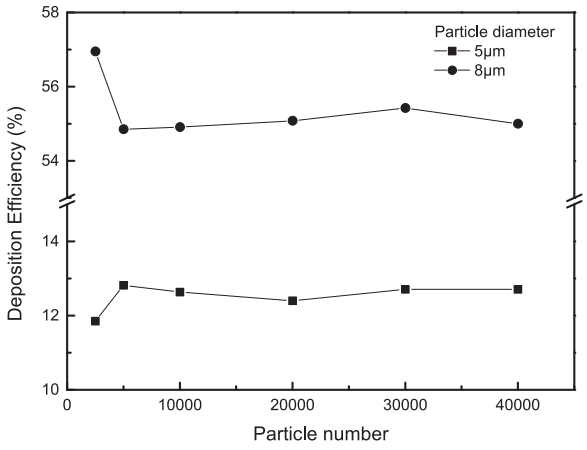


**(a) Particle number independence test;**

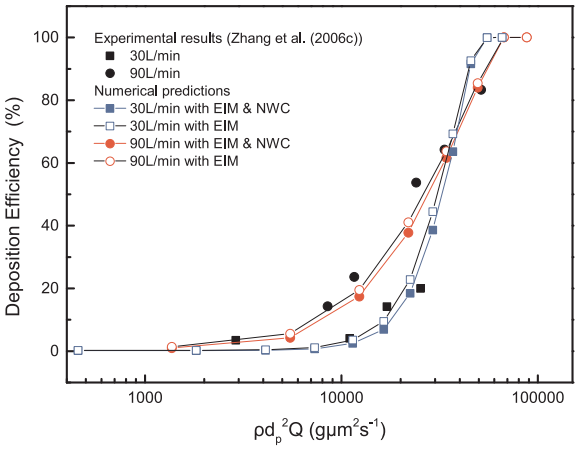


**(b) Comparison of DEs predicted by different models**

**Fig. 2.** Validation of particle transport and deposition: (a) particle number independence test; (b) comparison of DEs predicted by different models.

droplet density.

The governing equation for the heat transfer of the droplet is

$$\sum_{i=1}^{m} m_{d,i} c_{d,i} \cdot \Delta T = \pi d_d \lambda_g Nu (T_a - T_d) - \sum_{e=1}^{k} \iint_d n_e L_e dA \tag{26}$$

where $Nu$ is the Nusselt number defined as

$$Nu = (1 + \mathrm{Re}_d \mathrm{Pr})^{1/3} \max[1, \mathrm{Re}_d^{0.077}] \tag{27}$$

where $\mathrm{Re}_d$ is the Reynolds number of the droplet, and Pr is the Prandtl number.

### 2.4. Validation of aerosol transport and deposition

The independence of particle number was examined at 30 L/min for particles with diameters of 5 and 8 μm, as shown in Fig. 2(a). The particle density was 912 kg/m$^3$, which is the same as the experiment of Zhang et al. (2006c). The variations in DEs were less than 1% when the particle number was larger than 10 000. Thus, the droplet number of 10 000 was also adopted for the following simulations of the hygroscopic droplets. The DE is defined as:

$$\mathrm{DE} = \frac{m_{deposited}}{m_{total}} \times 100\% \tag{28}$$

where $m_{deposited}$ is the mass of the droplets / particles deposited on the airway surface, and $m_{total}$ is the mass of the droplets / particles entered the inlet.

Fig. 2(b) demonstrates the comparison of DEs between the results of different numerical models for discrete phase with experimental data (Zhang et al. 2006c) at 30 and 90 L/min. The time step for tracking the particles in these simulations was $10^{-5}$ s as

suggested by Matida et al. (2004). The predictions with NWC are generally in accordance with the experiment. It fits the experimental data well at flow rate of 30 L/min, and slightly underestimates the deposition efficiency at 90 L/min. The discrepancy could be caused by the smooth surface assumption used in the simulations. Because the airway model in the experiment was produced by Stereo-Lithography prototyping method with extra coating (Zhang et al. 2006c). However, the surface roughness of the airway model in the experiment is unknown. There is experimental evidence showing that rough surface can enhance particle deposition. For example, Kelly, Asgharian, Kimbell, and Wong (2004) carried out the micron particle deposition experiment in nasal replicas manufactured by different methods. The two replicas shared the same geometry, but the build layer thicknesses were different, i.e., 0.102 mm and 0.051 mm. The nasal airway model with thicker build layer, i.e., greater surface roughness, could have a DE value approximately 20% higher than the other model for the same inertial parameter $\rho d_p^2 Q$. Therefore, the effect of the surface roughness on DE may need further investigation.

Matida et al. (2004) reported that the DEs predicted without NWC had large discrepancy based on $k$-$\omega$ model. However, this difference is significantly reduced (see Fig. 2(b)) when the transition SST model is applied. A possible explanation is that the mesh size for the transition SST model is necessarily much smaller than that for the $k$-$\omega$ model. The transition SST model predicts the kinematic energy $k$ more accurately in the laminar sublayer. Thus, if the $k$-value is small, as it is the case in the laminar sublayer, (see Eq. (11)), the difference between isotropic and anisotropic eddy assumptions would be limited. The EIM with NWC model was selected for the final tracking method for the discrete phase, considering the existence of anisotropic eddy near the boundary.

A mouth piece with a diameter of 1.73 mm was used as the inlet in the experiment (Zhang et al., 2006c) as well as the numerical predictions in Fig. 2(b). However, Lin, Breysse, Laube, and Swift (2001) suggested that larger mouth piece could reduce the deposition in oral airway, especially for particles with diameters of 4 and 8 μm. Therefore, it was assumed that inlet for the air flow and droplets had the same diameter as the mouth for the simulations of the multicomponent droplet transport and deposition in the idealized MT airway in the following sections.

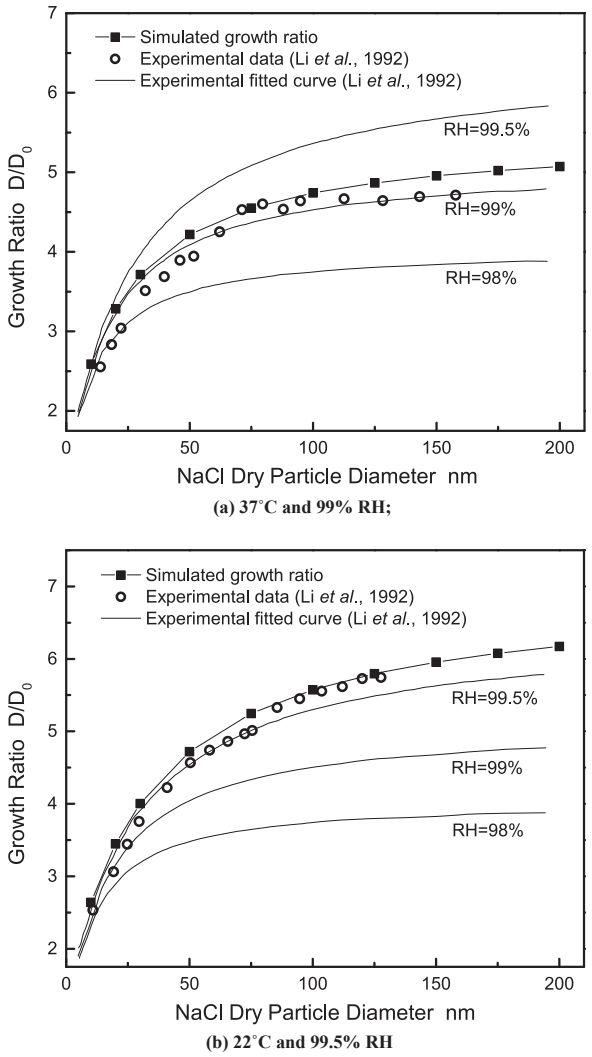


**Fig. 3.** Hygroscopic growth of dry NaCl particle: (a) 37°C and 99% RH; (b) 22°C and 99.5% RH Li et al. (1992).

**Table 2**
Environment and flow parameters.

| Parameters | Values | |
|---|---|---|
| | 37°C 99% RH | 22°C 99.5% RH |
| Flow temperature [K] | 310.15 | 295.15 |
| Reynolds number | 141 | 141 |
| NaCl density [kg/m$^3$] | 2165 | 2165 |
| Water density [kg/m$^3$] | 1000 | 1000 |
| Saturation pressure of water vapor [Pa] | 6279.2[a] | 2644.4[a] |
| Saturated vapor specific volume [m$^3$/ kg] | 22.742[a] | 51.445[a] |
| Wet air pressure [Pa] | 101325 | 101325 |
| Wet air density [kg/m$^3$] | 1.112 | 1.184 |
| Gas mean free path [m] | $6.8\times10^{-8}$ | $6.8\times10^{-8}$ |
| Molar mass of water [kg] | 0.01801528 | 0.01801528 |
| Molar mass of NaCl [kg] | 0.0584430 | 0.0584430 |
| Particle surface tension [N/m] | 0.07008 | 0.07008 |
| Particle temperature $T_d$ [K] | 310.15 | 295.15 |
| RH | 99% | 99.5% |
| Initial dry NaCl particle diameter [nm] | 10, 20, 30, 50, 75, 100, 125, 150, 175, 200 | |

[a] Yan et al. (2004).

### 2.5. Validation of multicomponent droplet – vapor interaction model

#### 2.5.1. Steady case: NaCl-Particle growth under high humidity conditions

Li, Montassier, and Hopke (1992) examined the growth of NaCl-particles with different sizes under different relative humidity (RH) conditions experimentally. In the experiment, the polydispersed aerosol particles were brought into the differential mobility analyzer (DMA), which classified the aerosols, only allowing the aerosols with designated diameter to pass. The identified aerosols were then directed into a wetted wall reactor, which ensured the aerosols to grow in the airflow with RH $>$ 99%. The length of the reactor could ensure that the growth of hygroscopic particles could achieve equilibrium states. After the growth in the reactor, the aerosols were entrained into the second DMA, and then the aerosol concentration was measured by a condensation nucleus counter (CNC). The last procedure was repeated several times with different selected aerosol diameters. Thus, the mean diameter of these aerosols which had absorbed moisture could be acquired from the fitted diameter distribution.

For the validation, the water activity coefficient $\gamma_w$ in the dilute NaCl solution is approximated by (Finlay, 2001)

$$\gamma_w x_w \approx 1 - \frac{i x_s}{x_w} \tag{29}$$

where $i$ is experimentally determined parameter called van't Hoff factor (1.85 for NaCl), and $x_w$ is the mole fraction of water.

For example, a dry NaCl particle was placed in an airstream with Re = 141, 37°C and RH = 99% (i.e., condition used in Fig. 3(a)) at the beginning of the simulation. The NaCl particle would gradually absorb water vapor from the air, and form an aerosol containing saturated NaCl solution with NaCl-crystal. As the aerosol kept absorbing water vapor, the mass of NaCl-crystal would decrease and the portion of the saturated NaCl solution would increase accordingly until the NaCl-crystal was fully dissolved. A similar assumption, i.e., solution with undissolved core, was also made by Hindle and Longest (2011) when simulating hygroscopic nanoparticles. Then the NaCl droplet continued to grow till the equilibrium state was achieved, and its diameter was recorded. During this simulation, rapid mixing was assumed, i.e., the negligible gradient of solution concentration in the droplet when interacting with the vapor.

Fig. 3 shows the diameter growth ratio of a dry NaCl particle, comparing experimental results and numerical predictions. The circles and solid lines are the experimental data and fitted curves for different RH-values (Li et al., 1992). The solid line with filled squares is the prediction from the multicomponent aerosol – vapor interaction model discussed above. The detailed environment and flow parameters used are summarized in Table 2. The predictions based on the numerical model of this study only have an approximately 0.1% to 0.2% RH discrepancy from the experimental data. In order to avoid oscillations of the particle / droplet components during the simulation, the time step of the discrete phase was reduced to $10^{-7}$ s.

The saturated vapor properties have a significant effect on the growth ratio of the hygroscopic particle; specifically, the mass fraction of the vapor in the air around the particle is crucial. Fig. 4 shows the simulated results using different saturated vapor properties for air at 37°C with RH = 99%. Property A is the same as used in Table 2, which are the exact values of 37°C (Yan, Yu & Wang, 2004), while Property B is the data interpolated from a property tables booklet (Cengel & Boles, 2010). In order to show the difference, the detailed values of these sets properties and calculated parameters based on these properties are listed in Table 3. It is surprising that the small change in the vapor mass fraction (0.0003) causes a significant difference in the particle growth ratio (1.45). Feng, Kleinstreuer, and Rostami (2015) also suggested that droplet-growth ratio is sensitive to small variations in the physical and chemical properties of water when validating the model for hygroscopic cigarette smoke particles.

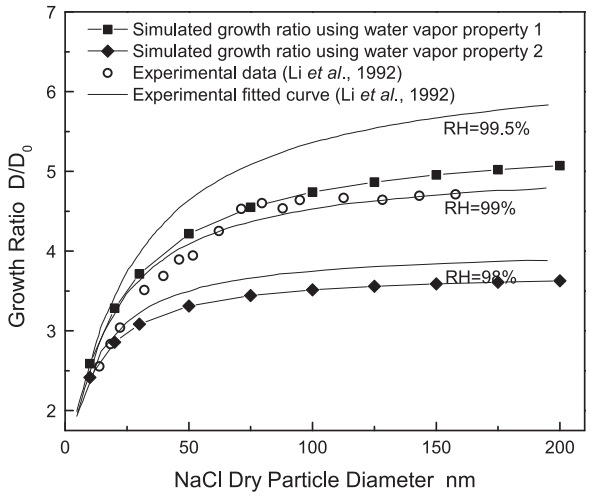


**Fig. 4.** Hygroscopic diameter growth of NaCl dry particle using different saturated vapor properties.

*2.5.2. Transient case: glycerol – droplet growth under transient humidity conditions*

Tu and Ray (2005) developed a novel method which could not only measure the size change of the droplet, but also can calculate the activity coefficient. During each experiment, a single pure glycerol droplet was suspended in a cylinder shape chamber via electrodynamical balance. The top and bottom plates of the chamber were maintained at 25 °C. The chamber was filled with dry air at the beginning. Then an aqueous solution of sodium chloride was inserted into the bottom of the chamber to modify the relative humidity in the chamber. The water vapor concentration increased slowly, and finally achieved a uniform steady distribution in the chamber. The glycerol droplet growth for three different droplets (i.e., #1 to #3) with the following initial radii, $R$, and final RH-values: (i) $R=11.95$ μm under final RH = 73%; (ii) $R=12.87$ μm under final RH = 87%; and (iii) $R=11.51$ μm under final RH = 87% were examined.

In order to examine the accuracy of the present model for transient conditions, the validations were carried out based on available experimental observations and simulation results (Tu & Ray, 2005; Zhang et al., 2012). Fig. 5 shows the ambient relative humidity evolution over time as measured plus curve – fitted computational results, which were used as boundary condition in the validation. For curve-fitting, exponential decay functions with multiple terms were employed, i.e.,

$$\mathrm{RH} = \alpha_0 + \alpha_1 e^{-t/t_1} + \alpha_2 e^{-t/t_2} + \alpha_3 e^{-t/t_3} \tag{30}$$

The water activity coefficient curve was in the form of van Laar equation:

$$\ln \gamma_w = \frac{C_1}{\left(1 + \frac{C_1}{C_2}\frac{x_w}{1-x_w}\right)^2} \tag{31}$$

where the constants $C_1 = -0.3049$, $C_2 = -0.8551$ are regressed by Ray and Tu (2005) based on their experimental data.

Fig. 6(a) and (b) provide the comparisons of droplet growth and product of water activity coefficient and water molar fraction $\gamma_w x_w$ between the numerical prediction of current model (in solid lines) with ± 2% RH error bar (in dash lines), simulations of Zhang et al. (2012) (in dash dot lines) and experimental data (in scattered points) (Ray and Tu, 2005). Note that the $\gamma_w x_w$ data is not provided in the results of Zhang et al. (2012). Despite small discrepancies exist in Fig. 6(a), both droplet diameter and $\gamma_w x_w$ variations

**Table 3**
Vapor properties and related parameters.

| | Parameters | Values | |
|---|---|---|---|
| | | Property A[a] | Property B[b] |
| Parameters from handbook | Saturation pressure of water vapor [Pa] | 6279.2 | 6331.5 |
| | Saturated vapor specific volume [$m^3$/ kg] | 22.742 | 22.929 |
| Calculated parameters | Vapor partial pressure of 99% RH [Pa] | 6216.408 | 6268.185 |
| | Dry air partial pressure of 99% RH [Pa] | 95108.592 | 95056.815 |
| | Wet air pressure [Pa] | 101325 | 101325 |
| | Vapor density [kg/$m^3$] | 0.043531791 | 0.043176763 |
| | Wet air density [kg/$m^3$] | 1.112089612 | 1.111152862 |
| | Vapor mass fraction of 99% RH air [kg /$m^3$] | 0.03914414 | 0.038857627 |

[a] Yan et al. (2004).
[b] Boles and Cengel (2010).

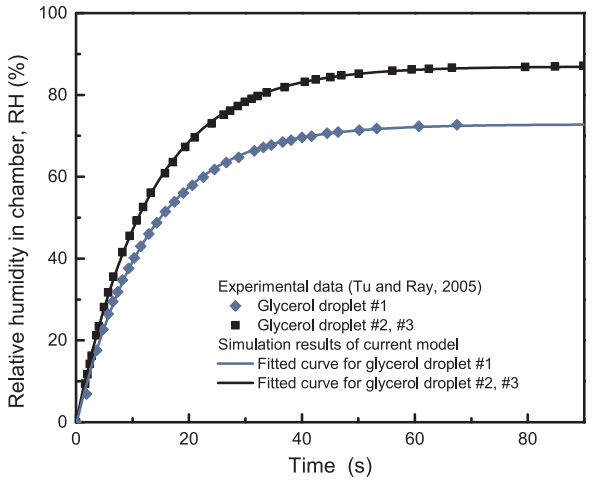


**Fig. 5.** Relative humidity evolution in chamber for the unsteady glycerol-water droplet growth.

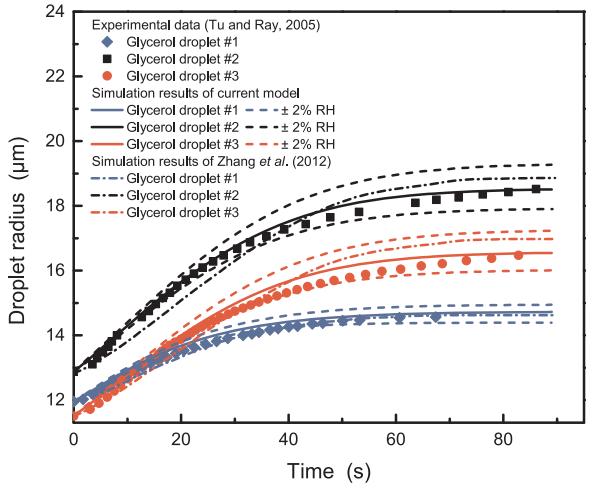


**(a) The variation of droplet radius over time**

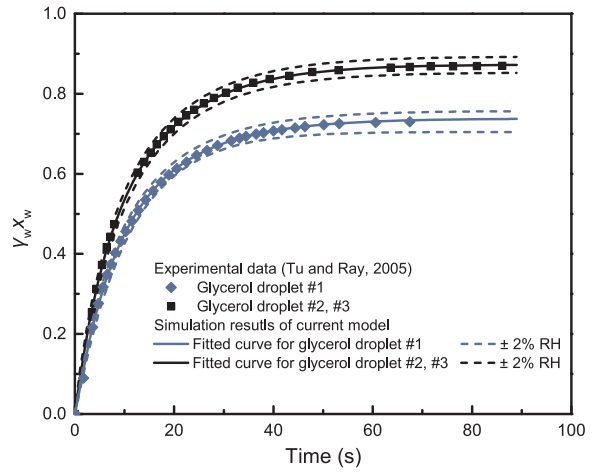


**(b) The variation of product of water activity coefficient and mole fraction of water in the droplet over time**

**Fig. 6.** Validation of transient hygroscopic growth of glycerol-water droplet: (a) the variation of droplet radius over time; (b) the variation of product of water activity coefficient and mole fraction of water in the droplet over time.

**Table 4**
Inlet and boundary conditions applied in the simulations.

| Conditions | Flow rate (L/min) | Inlet RH (%) | Boundary wetness |
|---|---|---|---|
| A | 15 | 30 | wet |
| B | 30 | 30 | wet |
| C | 45 | 30 | wet |
| D | 60 | 30 | wet |
| E | 60 | 30 | dry |
| F | 60 | 80 | wet |

over time fit the experimental data well.

### 2.6. Simulation setup

In light of the dilute flow assumption, one way coupling was applied during the simulation of the hygroscopic droplet transport and deposition in the simple MT model. The fluid flow was simulated using ANSYS Fluent 14.5 (ANSYS, Inc., Canonsburg, PA) until the residual was less than $10^{-4}$. The initial probability density distributions of the droplets at the inlet were proportional to the flow velocity profiles. A C++ program was coded to generate the random droplet distribution with determined probability density. The initial velocity and temperature (37 °C) of the droplets were set the same as the fluid via UDF. For each case, 10, 000 droplets were released at the inlet surface. The deposition was assumed to occur once the droplet collided with the airway surface. Droplet size and spatial location were recorded when the droplet deposited on the boundary or escaped from the outlet. The hygroscopic aerosol – vapor interaction, droplet transport, e.g., drag force, fluctuating velocity, etc., were programmed and implemented by the UDF.

In order to investigate the factors influencing the hygroscopic droplet transport and deposition, simulations under six different conditions were carried out, as shown in Table 4. The six conditions aim to examine three different effects: Condition A to D investigate the effect of flow rate; Condition D and E study the effect of boundary wetness; Condition D and F examine the effect of inlet RH-value. The wet boundary was assumed having a RH-value of 99.5% at the surface. Transport and deposition of different diameters of droplets, e.g., 2.5, 3.75, 5, 6.25 etc., up to 20 μm were simulated for each conditions until the DE achieved 100%. Each droplet contains four components, i.e., water, ethanol, NaCl and fluorescein. The mass ratios of the components were fixed as water: ethanol: NaCl: fluorescein =400:100:100:2.5. Due to the low solubility of fluorescein in water (1 mg / ml), the fluorescein was considered as a component that only affects the droplet mass, diameter and heat capacity. If the droplet evaporates completely, i.e., only NaCl and fluorescein remains, the solid particle's diameter is 44.3% of the original droplet. The temperatures of the air and the airway were assumed at 37 °C.

## 3. Results & discussion

### 3.1. Velocity distributions

The airflow field, including the velocity and kinetic energy distributions in the simple MT model with an inlet smaller than the mouth opening, has been analyzed by Zhang et al. (2006c) at flow rates of 30 L/min and 90 L/min. In light of the limited air density change caused by the RH difference (i.e., Conditions D to F), the velocity distributions would be similar under different RH conditions. Thus, Fig. 7 illustrates the velocity distributions in the symmetrical plane and at the outlet of the simple airway for Conditions A to D. It is clear that the four conditions with different flow rates share similar airflow structures. While the air-velocity at the inlet is the lowest, it increases as the cross-sectional area gradually decreases. The bend tube causes a skewed velocity distribution, which has a higher velocity closer to the A'-side of the MT model. As a result, it forms two symmetric vortices in the radial plane that can enhance the species transport of water vapor.

### 3.2. Relative humidity distributions

The RH distributions for the symmetrical plane and the outlet of MT model for Condition A to D and Condition F are illustrated in Fig. 8(a) to (e). There is no other effect could influence the RH under Condition E, the RH remains at 30%, and hence, it is not illustrated in Fig. 8. It can be seen that the curved pipe causes asymmetric distribution of the RH. However, the extent of the asymmetry varies with inlet conditions. The asymmetry is obvious, if the airway inlet and boundary have large RH difference. For example, the gradient of the RH is notable in Fig. 8(a) to (d), because the RHs of the inlet and boundary are 30% and 99.5% under Condition A to D, respectively. While the RH distribution is mostly symmetric along the path of MT airway in Fig. 8(e) due to the small RH difference between the inlet (80%) and boundary (99.5%). For the large inlet and boundary RH difference condition, even though the RH-values are different at the outlets for different flow rates, the shapes of the RH distribution are similar: The front side towards the oral cavity has higher RH, and the back side is comparatively lower. As mentioned above, the hygroscopic growth of the droplet is closely related to the RH-value. Therefore, the RH distribution could affect the droplet size and its further trajectory. In addition, droplets, which have the same Stokes number based on different combinations of initial diameter and inlet flow rate, may behave differently, e.g., droplet trajectory, DE, etc., due to the RH distribution.

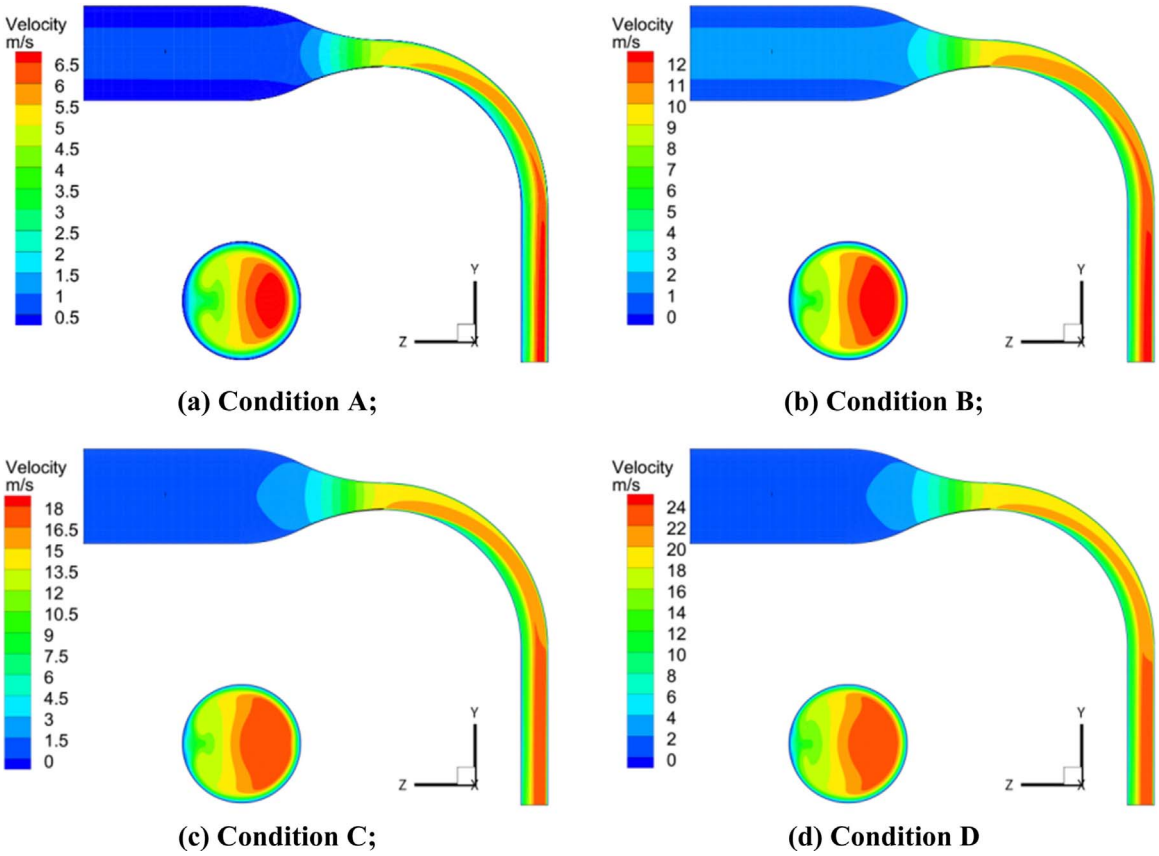


**Fig. 7.** Velocity distributions of the symmetrical plane and outlet of the MT model for different flow rate conditions: (a) Condition A; (b) Condition B; (c) Condition C; (d) Condition D.

### 3.3. Deposition efficiencies

Fig. 9 depicts the deposition efficiencies of the hygroscopic droplets in the MT model for different flow rate, boundary and inlet humidity conditions.

Fig. 9(a) illustrates the flow rate effect on the DEs of the hygroscopic droplets. Stokes number (*St*) for graphing the deposition results is defined as

$$St = \frac{\rho_d d_d^2 U}{18\mu D} \tag{32}$$

where $U$ is the mean inlet velocity and $D$ is the inlet diameter.

It is interesting that the DE at low flow rate is higher than that at high flow rate for the same Stokes number. The increase in DE could be caused by enhanced hygroscopic growth of the droplets. The average value of RH in the airway is higher at lower flow rate condition (see Fig. 8). Thus, the droplets have higher possibility to interact with high RH air. The reduced air velocity also increases the interaction time of the droplet with the humid air. Therefore, the droplets can achieve higher mass after hygroscopic growth.

Generally, the droplet DEs under Condition D are higher, compared to Condition E for the same flow rate at 60 L/min in Fig. 9(b). However, the increase of DEs due to hygroscopic growth varies with Stokes numbers (i.e., different droplet initial diameters). The wet wall could enhance the DE by approximately 4.6% in the *St* range of $0.1 < St < 0.3$, while this enhancement is not apparent for small or large *St*-value regions, i.e., $St < 0.1$ or $St > 0.3$. Similarly, this effect can increase the DE by 7% at 15 L/min (not plotted).

The inlet air humidity has significant impact on the droplet DE. The DE under Condition F (i.e., inlet RH = 80%) could be 30% (Stokes number range from 0.01 to 0.03) higher than simulations under Condition D (i.e., inlet RH = 30%) shown in Fig. 9(b), when the two cases shared the same flow rate at 60 L/min and wet wall condition. Considering an equilibrium status of the NaCl – water droplet in a constant RH environment, the mass fraction of the water vapor near the droplet surface would equal to the value in the surrounding air, i.e.,

$$Y_{w,surf} = \gamma_w x_w K_w \frac{P_{vw,sat}(T_d)}{\rho R_w T_d} = \gamma_w x_w K_w \frac{\rho_{vw,sat}}{\rho} = RH \frac{\rho_{vw,sat}}{\rho} = Y_{w,\infty} \tag{33}$$

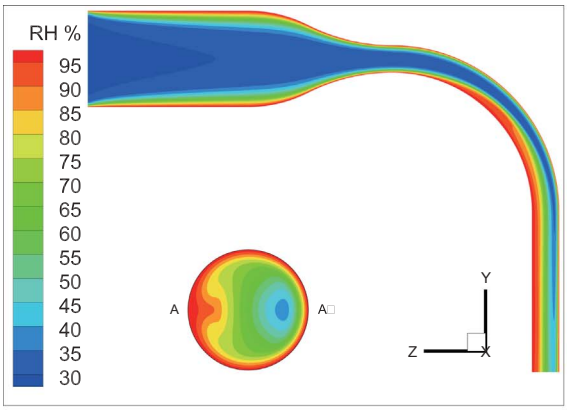


**(a) Condition A, volume-averaged RH = 51.0%, average RH = 74.4% on outlet surface;**

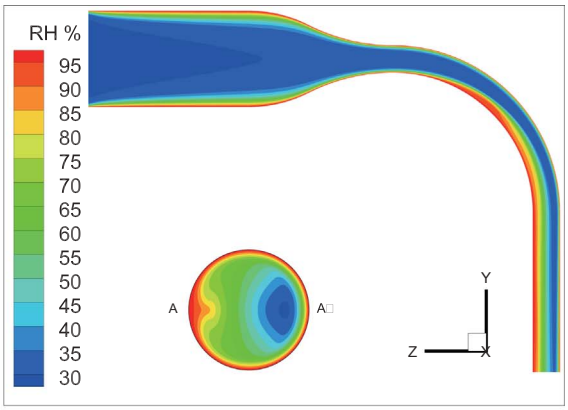


**(b) Condition B, volume-averaged RH = 46.3%, average RH = 64.8% on outlet surface;**

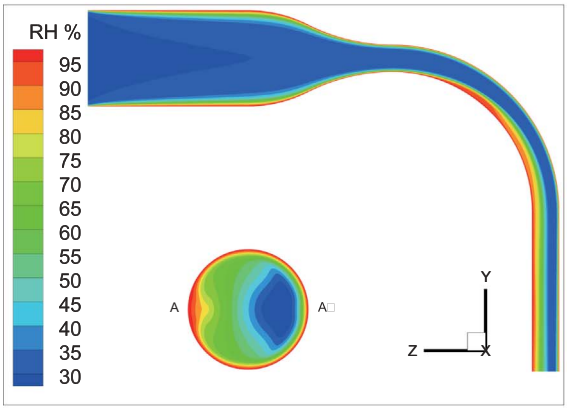


**(c) Condition C, volume-averaged RH = 43.1%, average RH = 60.5% on outlet surface**

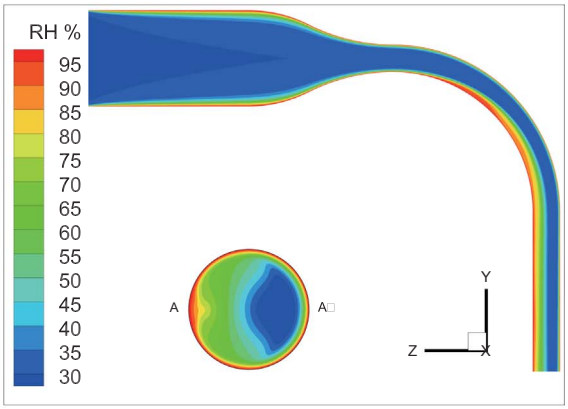


**(d) Condition D, volume-averaged RH = 41.6%, average RH = 57.4% on outlet surface;**

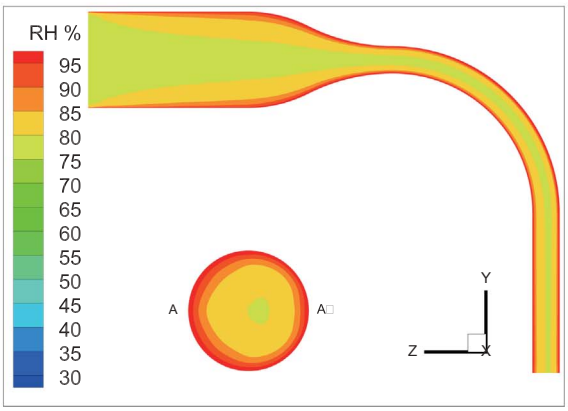


**(e) Condition F, volume-averaged RH = 83.2%, average RH = 86.1% on outlet surface**

**Fig. 8.** RH distributions of the symmetrical plane and outlet of the MT model for different flow rate conditions with wet boundary: (a) Condition A, volume-averaged RH = 51.0%, average RH = 74.4% on outlet surface; (b) Condition B, volume-averaged RH = 46.3%, average RH = 64.8% on outlet surface; (c) Condition C, volume-averaged RH = 43.1%, average RH = 60.5% on outlet surface; (d) Condition D, volume-averaged RH = 41.6%, average RH = 57.4% on outlet surface; (e) Condition F, volume-averaged RH = 83.2%, average RH = 86.1% on outlet surface.

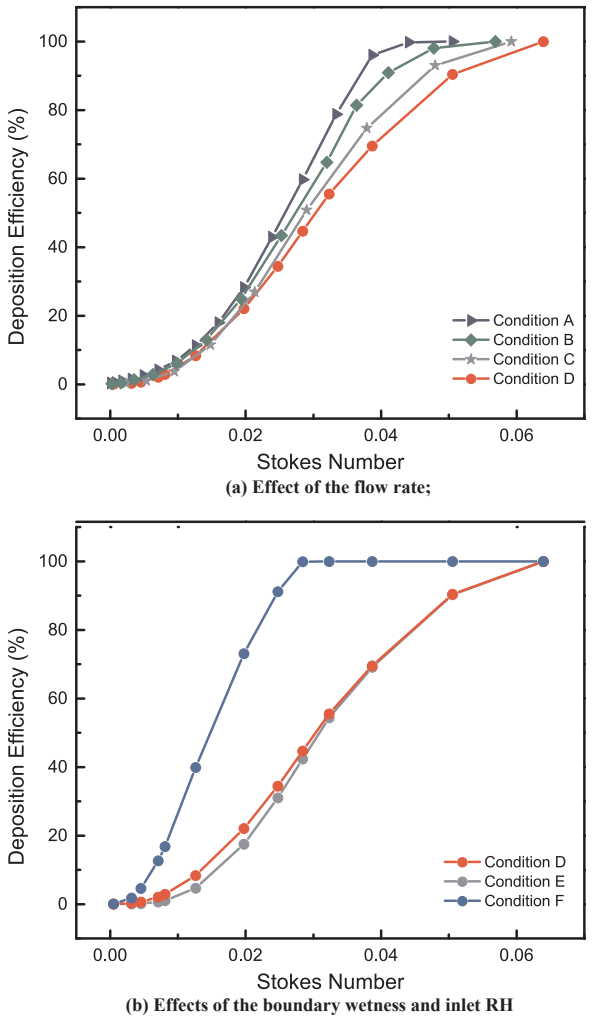


**Fig. 9.** Comparison of deposition efficiency of hygroscopic droplet in the mouth-throat airway under different conditions: (a) effect of the flow rate; (b) effects of the boundary wetness and inlet RH.

Thus,

$$\gamma_w x_w K_w = RH \tag{34}$$

Experimental observation (Tang et al., 1977) indicated that the deliquescence point for the NaCl aerosol was approximately RH = 76% at 25 ˚C, which was similar to the value of 75.3% for the bulk solution (Robinson & Stokes, 1970). Cruz and Pandis (2000) reported that the threshold RH for a 100 nm NaCl aerosol to grow was 75% at 22–26 ˚C condition.

The threshold RH estimated based on Eqs. (25) and (34) is approximately 79% for a 100 nm NaCl aerosol at 25 ˚C when using the $\gamma_w x_w$ result under the condition of saturated solution of NaCl. This small discrepancy could be caused by the simplified calculation used in Eq. (29). Hence, the great DE difference between the RH = 30% and 80% inlet conditions is caused by the interaction of the multicomponent in the droplet and the surrounding water vapor. The droplet shrunk in the main stream under inlet RH = 30% condition (Condition D), while it would achieve an equilibrium status as a droplet (still the ethanol would evaporate) when moving in the high humidity flow (i.e., RH = 80%, Condition E). Therefore, an accurate prediction of the fluid phase RH distribution is vital for a correct simulation of hygroscopic droplet transport and deposition.

Hoffman, Lin, Wu and Tawhai (2014) numerically examined the temperature and RH distributions during the transient breathing condition in a realistic airway including the thermal property of the airway tissue. The results indicated that the temperature and RH of the airway were lower than 37 ˚C and 99.5%, respectively. The differences were up to 5 ˚C in temperature and 3% in RH. As discussed above, the hygroscopic growth is sensitive to the temperature and RH variations. Thus, such effects on droplet hygroscopic growth and their effects on further droplet transport and deposition still need extra investigation.

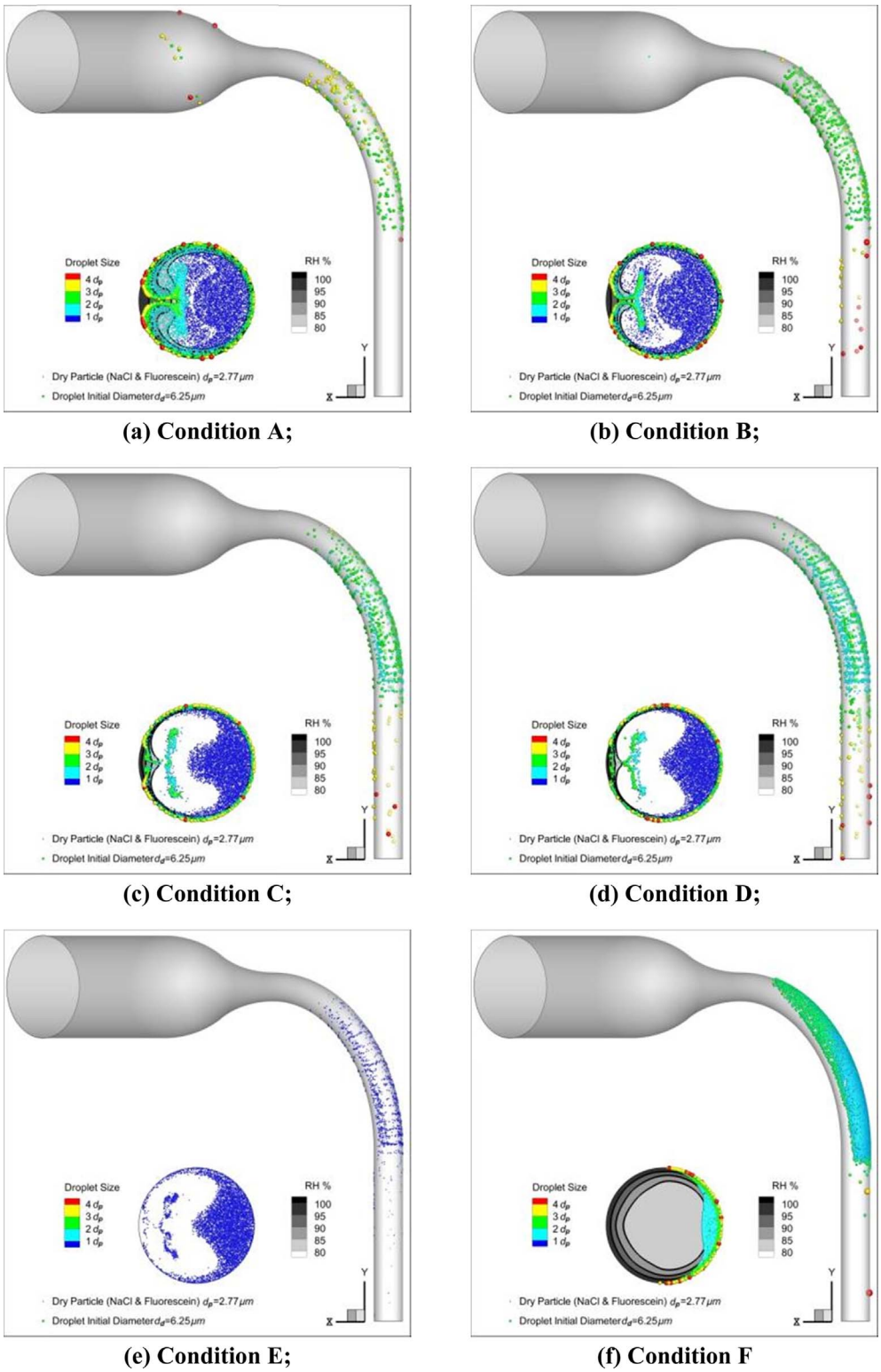


**Fig. 10.** Final diameters and locations of hygroscopic droplets under different conditions: (a) Condition A; (b) Condition B; (c) Condition C; (d) Condition D; (e) Condition E; (f) Condition F.

### 3.4. Deposition patterns and escaped droplets and particles distributions

Fig. 10(a) to (f) illustrate the deposition patterns and distributions of droplets at outlet with initial diameter of 6.25 μm under Condition A to F. The sizes of the droplets have been enlarged in Fig. 10 to give a clear view. Two size references, i.e., 6.25 μm and 2.77 μm as the diameters of the initial droplet and its solid core, which contains only NaCl and fluorescein, are plotted on the left bottom of each figure. The RH distributions at airway outlet are demonstrated by greyscale contours to highlight the regions with RH > 80%. Fig. 11 shows the variations in the average growth ratios of deposited and escaped droplets as well as DEs under those conditions. The average growth ratio used in Fig. 11 is defined as the ratio of the average diameter of the deposited or escaped droplets to the diameter of the *dry* particle (i.e., contains only NaCl and fluorescein) for the same condition.

#### 3.4.1. Effect of the flow rate

As the fluid velocity increases, the momentum of the droplets increases consequently. Thus, more deposition occurred on the A' side surface of the curved pipe, as shown in Fig. 10(a) to (d). As mentioned above, the diameters of the droplets in the main flow would rapidly decrease due to evaporation in the low RH-value (30%) at the beginning of the oral cavity. Similar case, i.e., the evaporation of saline droplets, can refer to the numerical study of Zhang et al. (2006a). The diameter of dry particle of the 6.25 μm droplet is 2.77 μm (e.g., see Fig. 10(e) for the uniformly evaporated particles). However, the average diameter of deposited droplets under wet wall, RH = 30% and different flow rate conditions were obviously larger (see Fig. 10(a) to (d)). The growth of the deposited droplets suggests the interaction of droplets with the high RH air. However, the extent of the hygroscopic growth varies with flow rate conditions.

The growth ratio of deposited droplets decreases with a higher flow rate for the same droplet initial diameter (in black solid lines), as shown in Fig. 11(a). It also decreases with a larger droplet initial diameter under condition of equal flow rate. This indicates that

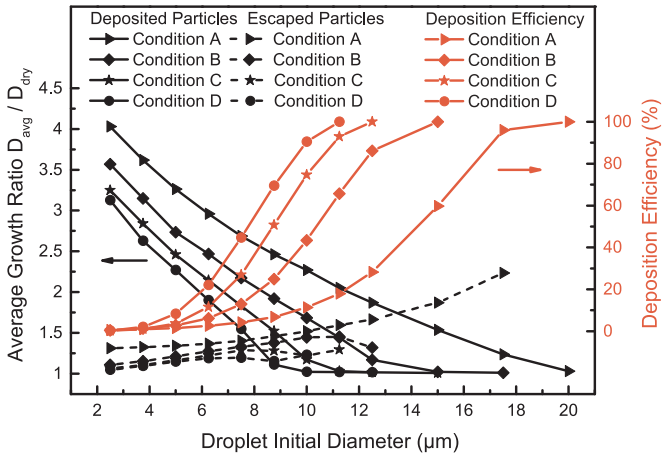


**(a) Effect of the flow rate;**

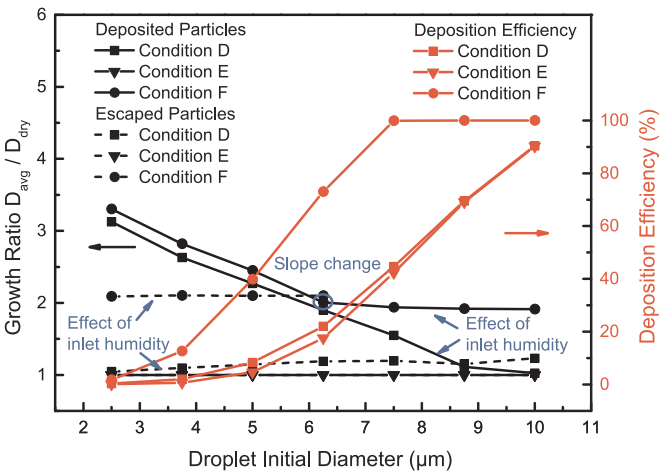


**(b) Effects of the boundary wetness and inlet RH**

**Fig. 11.** The variations of diameters of deposited and escaped droplets and DEs under different conditions: (a) effect of the flow rate; (b) effects of the boundary wetness and inlet RH.

high droplet momentum is required for depositing under low flow rate or small droplet condition. Thus, the growth ratios are large when the DE-values are relatively small. As the DE reaches 80%, the growth ratio drops down to 1 and its slope has a sharp change. It suggests that the droplets obtained high momentum that can deposit even without hygroscopic growth.

For the droplets escaped from the outlets, the ones with increased sizes only appeared in the region near the boundary, except those were drawn into the center by the secondary flow. In contrast, the diameters of most of the droplets / particles in the tube center were still small. This shows the hygroscopic growth of the droplet closely relates to the local RH-value, especially the regions with RH higher than the threshold. More specifically, the hygroscopic growth of the NaCl particle requires a humid environment with RH > 80% as described above, which only exists in the near – wall region. Thus, droplets and particles absorbed water vapor in this region and consequently achieved larger sizes. It indicates that the hygroscopic growth is a local behavior happened mostly in the high RH region. The RH criterion is determined by the solubilities of the components in the droplet or particle (see Eq. (34)).

The average growth ratio of escaped droplets slowly increases with a larger droplet initial diameter at the four flow rates (in dash lines) in Fig. 11(a). Obviously, the increased droplet momentum causes that the DE increases with increased droplet diameter. Thus, more droplets deposited on the A' side surface of the curved pipe caused by inertial impact. At the same time, the escaped droplets moved closer toward A' side boundary at the outlet because of increased momentum and centrifugal force. Therefore, these droplets could interact with higher RH air, and hence, their diameters were comparatively larger. On the other hand, the average growth ratio of escaped droplets decreases with a higher flow rate for the same droplet size. But the values of the growth ratios are similarly small ranging from 1 to 1.5 under most conditions. The difference in these growth ratios is caused by the RH difference in the airway. More specifically, because the airway had higher average RH under lower flow rate condition (see Fig. 8), the average size of the escaped droplets was larger accordingly. However, the majority of the escaped droplets located in the center of the outlet, where the RH-value was relatively low. Thus, the average diameters of the escaped droplets are commonly small.

### 3.4.2. Effect of boundary wetness

Fig. 10(d) and (e) compare the deposition pattern and distribution of droplets at outlet under Condition D and E. The two conditions shared the same flow rate at 60 L/min and inlet RH distribution but different boundary relative humidity values, i.e., RH = 99.5% and RH = 0% for Condition D and E, respectively. Although the spatial distributions of the deposited and escaped droplets were similar, the diameters of these droplets had significant difference. All droplets evaporated and formed solid particles containing only NaCl and fluorescein under Condition E in Fig. 10(e), while the average diameters of the deposited and escaped droplets under Condition D were larger than that of the droplets under Condition E by 90.1% and 19.0%, respectively (see Fig. 11(b)). However, the difference in DE under these two conditions, i.e., 4.6%, is not as notable as the difference in droplet size.

The growth ratios of deposited and escaped droplets are all equal to 1 under Condition E when the boundary is dry in Fig. 11(b). It verifies that the droplets evaporate in the air with RH = 30%. Even though the difference in the growth ratios under Condition D and E is relatively large (e.g., larger than 0.5 until the droplet initial diameter increases to 7.5 μm), the change in deposition pattern is not apparent (see Fig. 10(d) and (e)). This suggests that the hygroscopic growth of the droplet under the high flow rate condition happened in the region close to its final deposition location, i.e., the high RH area near the airway boundary. Otherwise, the droplet trajectories and the according deposition pattern as well as the distribution at the outlet should have obvious change, if the hygroscopic growth of the droplet occurred in the mainstream.

### 3.4.3. Effect of the inlet RH

Fig. 10(d) and (f) illustrate the inlet RH effect on the transport and deposition of hygroscopic droplets. The droplets can maintain its size in the high RH air flow (i.e., RH = 80%) under Condition F rather than evaporate under the low RH condition, i.e., Condition A to E. The hygroscopic growth of the droplets in high RH airflow, i.e., Condition F, significantly changes the deposition pattern: concentrated deposition occurred on the surface on A' side of the MT-section in Fig. 10(f) rather than scattered deposition, as shown in Fig. 10(d).

The average growth ratio of deposited droplets under Condition F decreases with the increase of droplet initial diameter (in solid line) at the beginning in Fig. 11(b). It shares similar value and slope as the average growth ratio for Condition D at first. However, the slope of the average growth ratios curve for Condition F becomes flattened when the initial droplet is larger than 6.25 μm (see the blue circle in Fig. 11(b)). After this point, the DE under Condition F reaches 100%, and the growth ratio barely changes. It suggests that the droplets achieve the equilibrium status in the mainstream, and the droplet – vapor interaction has limited effect on the droplet when travelling through the region with RH gradient before depositing on the boundary.

The high inlet RH also has a pronounced influence on the droplet distribution at outlet as shown in Fig. 10(f). The increased droplet mass caused higher centrifugal force that moved the droplet toward A' side. Besides, it reduced the secondary flow effect on the circumferential droplet movement. Thus, the distribution of the droplets is more concentrate on the A' side at the outlet. It is obviously that the sizes of the escaped droplets are larger than other conditions in Fig. 10(a) to (e).

It is interesting to find that a high inlet RH distinctly increases the average growth ratio of escaped droplet. The average growth ratios under Condition F (inlet RH = 80%) are approximately 2.1, which are higher than that under Condition D (inlet RH = 30%) by 1. This value is similar to the average growth ratios of deposited droplets under the same Condition F when the DE arrives at 100% (i.e., droplet initial diameter larger than 6.25 μm). It can be concluded that an inlet RH higher than the growth threshold can elevate the average size of the droplet.

This characteristic could be beneficial for targeted drug delivery. For example, assuming NaCl is the main component of a drug particle. The final droplet diameter in the lower airway is preferred larger than 2.5 μm for the delivery in the alveolar region as suggested by Hindle, Longest and Tian, (2014). If 2.5 μm is the designated final droplet diameter, the initial diameter of the NaCl

particle would be roughly 420 nm when considering that the growth ratio of NaCl at RH = 99.5% is approximately 6 (see Fig. 3). This diameter is smaller than 0.9 μm, which is the optimal value suggested by Longest, Tian, and Hindle (2011) for aerosols to penetrate human upper airway. The transport of the particle with diameter of 420 nm is affected by Brownian motion, which can increase the deposition in the upper airway. Thus, a high inlet RH, e.g., RH = 80%, can increase the average droplet diameter and may improve the delivery efficiency. Similarly, if the initial particle contains non-hygroscopic component, e.g., budesonide (density of 1000 kg/m$^3$ used by Tian et al. (2014)), and assumes that the mass ratio of NaCl to budesonide is 1:1, the initial diameter of the particle would be approximately 610 nm to achieve a final diameter of 2.5 μm at RH = 99.5%. Thus, a high inlet RH may facilitate elevating the average diameter via hygroscopic growth to reduce the deposition in upper airway.

## 4. Conclusions

The interactions, transport and deposition of hygroscopic droplets containing four components, i.e., water, NaCl, ethanol and fluorescein, in a simple mouth-throat model under laminar-to-turbulent flow conditions have been analyzed. The multicomponent aerosol – vapor interaction model has been validated, subject to steady and transient conditions, with different solutes. The effects of the inlet flow rate, RH and wet or dry walls on the droplet deposition efficiency and deposition pattern as well as droplet distribution and final droplet size at the outlet have been analyzed. The following conclusions can be drawn:

(1) The hygroscopic growth of NaCl particle is sensitive to the saturation pressure of water vapor in the air. A small change in pressure (say, 52.3 Pa) can cause a large difference in particle growth ratio (up to 1.45).
(2) The inhalation flow rate not only affects the velocity of the droplets, but also changes the RH distribution in the airway for the wet boundary condition. A high flow rate reduces the average RH and shortens the droplet-vapor interaction time. Nevertheless, the deposition efficiency of the hygroscopic droplet still increases with higher flow rate. In turn, the average growth ratio of deposited droplets decreases with higher flow rate. The average growth ratio of escaped droplets also decreases with higher flow rates, but increases with larger droplet initial diameters.
(3) A wet airway-wall increases the DE for an inlet RH of 30% when compared to the dry boundary condition. The maximum increase in DE is 4.6% at 60 L/min. However, the average growth ratios of deposited droplets under wet boundary conditions are 2.1 to 0.5 times larger than that under dry walls within the droplet initial diameter range from 2.5 μm to 7.5 μm, respectively. The increase in average growth ratio of deposited droplets is not apparent ( < 0.3).
(4) The inlet RH could significantly change droplet transport and deposition due to hygroscopic growth, especially when it is larger than the RH threshold for the hygroscopic component. A high inlet RH, e.g., RH = 80% in this study, can increase the DE by 30% at 60 L/min, compared to the case with inlet RH = 30%. It generates concentrated deposition in the curved MT-section and moves the droplets toward the rear side of the MT model at the outlet. A high inlet RH can elevate the growth ratios of deposited and escaped droplets at the same time. This effect could be utilized to reduce the deposition caused by Brownian motion in the upper airway when the initial diameter of the aerosol is too small.

## Acknowledgements

The authors gratefully acknowledge the financial support of the National Natural Science Foundation of China(grant No. 51606041), National Natural Science Foundation of Jiangsu Prov. (grant No. BK20160688). The experience gained by the first author, Xiaole Chen, as a CSC-supported Visiting Student in the Computational Multi-Physics Lab (MAE Dept., NC State University, Raleigh, USA. http://www.mae.ncsu.edu/cmpl/) is also acknowledged.

## References

Allen, M. D., & Raabe, O. G. (1985). Slip correction measurements of spherical solid aerosol particles in an improved Millikan apparatus. *Aerosol Science and Technology*, *4*, 269–286.
Bird, R. B., Stewart, W. E., & Lightfoot, E. N. (1960). *Transport phenomena* Madison, USA: John Wiley Sons.
Cengel, Y. A., & Boles, M. A. (2010). *Thermodynamics: An Engineering Approach* (7th ed.) New York, NY, USA: McGraw-Hill.
Clift, R., Grace, J. R., & Weber, M. E. (1978). *Bubbles, drops, and particles* New York, NY, USA: Academic Press.
Cruz, C. N., & Pandis, S. N. (2000). Deliquescence and hygroscopic growth of mixed inorganic-organic atmospheric aerosol. *Environmental Science Technology*, *34*, 4313–4319.
Feng, Y., Kleinstreuer, C., & Rostami, A. (2015). Evaporation and condensation of multicomponent electronic cigarette droplets and conventional cigarette smoke particles in an idealized G3–G6 triple bifurcating unit. *Journal of Aerosol Science*, *80*, 58–74.
Feng, Y., Kleinstreuer, C., Castro, N., & Rostami, A. (2016). Computational transport, phase change and deposition analysis of inhaled multicomponent droplet–vapor mixtures in an idealized human upper lung model. *Journal of Aerosol Science*, *96*, 96–123.
Ferron, G., Kreyling, W., & Haider, B. (1988). Inhalation of salt aerosol particles—II. Growth and deposition in the human respiratory tract. *Journal of Aerosol Science*, *19*, 611–631.
Finlay, W. H. (2001). *The mechanics of inhaled pharmaceutical aerosols: an introduction* New York, NY, USA: Academic Press.
Fluent 14.5 users guide (2012). ANSYS Inc., Canonsburg, PA, USA
Fuchs, N. A., & Sutugin, A. G. (1969). *Highly dispersed aerosols* Michigan: Ann Arbor Science Publishers.
Ghahramani, E., Abouali, O., Emdad, H., & Ahmadi, G. (2014). Numerical analysis of stochastic dispersion of micro-particles in turbulent flows in a realistic model of human nasal/upper airway. *Journal of Aerosol Science*, *67*, 188–206.
Gosman, A., & Loannides, E. (1983). Aspects of computer simulation of liquid-fueled combustors. *Journal of Energy*, *7*, 482–490.
Javaheri, E., & Finlay, W. H. (2013). Size manipulation of hygroscopic saline droplets: Application to respiratory drug delivery. *International Journal of Heat and Mass Transfer*, *67*, 690–695.
Kelly, J. T., Asgharian, B., Kimbell, J. S., & Wong, B. A. (2004). Particle deposition in human nasal airway replicas manufactured by different methods. Part I: Inertial

regime particles. *Aerosol Science and Technology*, *38*, 1063–1071.
Kim, J., Moin, P., & Moser, R. (1987). Turbulence statistics in fully developed channel flow at low Reynolds number. *Journal of Fluid Mechanics*, *177*, 133–166.
Li, W., Montassier, N., & Hopke, P. (1992). A system to measure the hygroscopicity of aerosol particles. *Aerosol Science and Technology*, *17*, 25–35.
Lin, T.-C., Breysse, P. N., Laube, B. L., & Swift, D. L. (2001). Mouthpiece diameter affects deposition efficiency in cast models of the human oral airways. *Journal of Aerosol Medicine*, *14*, 335–341.
Longest, P. W., & Kleinstreuer, C. (2005). Computational models for simulating multicomponent aerosol evaporation in the upper respiratory airways. *Aerosol Science and Technology*, *39*, 124–138.
Longest, P. W., McLeskey, J. T., Jr, & Hindle, M. (2010). Characterization of nanoaerosol size change during enhanced condensational growth. *Aerosol Science and Technology*, *44*, 473–483.
Longest, P. W., & Hindle, M. (2011). Numerical model to characterize the size increase of combination drug and hygroscopic excipient nanoparticle aerosols. *Aerosol Science and Technology*, *45*, 884–899.
Longest, P. W., Tian, G., & Hindle, M. (2011). Improving the lung delivery of nasally administered aerosols during noninvasive ventilation—an application of enhanced condensational growth (ECG). *Journal of Aerosol Medicine and Pulmonary Drug Delivery*, *24*, 103–118.
Longest, P. W., & Xi, J. (2008). Condensational growth may contribute to the enhanced deposition of cigarette smoke particles in the upper respiratory tract. *Aerosol Science and Technology*, *42*, 579–602.
Matida, E., Finlay, W., Lange, C., & Grgic, B. (2004). Improved numerical simulation of aerosol deposition in an idealized mouth–throat. *Journal of Aerosol Science*, *35*, 1–19.
Menter, F. R., Langtry, R., & Völker, S. (2006). Transition modelling for general purpose CFD codes. *Flow, Turbulence and Combustion*, *77*, 277–303.
Menter, F. R., Langtry, R., Likki, S., Suzen, Y., Huang, P., & Völker, S. (2006). A correlation-based transition model using local variables—Part I: Model formulation. *Journal of Turbomachinery*, *128*, 413–422.
Morsi, S., & Alexander, A. (1972). An investigation of particle trajectories in two-phase flow systems. *Journal of Fluid Mechanics*, *55*, 193–208.
Nenes, A., Pandis, S. N., & Pilinis, C. (1998). ISORROPIA: A new thermodynamic equilibrium model for multiphase multicomponent inorganic aerosols. *Aquatic Geochemistry*, *4*, 123–152.
Robinson, R. A., & Stokes, R. H. (1970). *Electrolyte solutions* London: Butterworths.
Tang, I., Munkelwitz, H., & Davis, J. (1977). Aerosol growth studies—II. Preparation and growth measurements of monodisperse salt aerosols. *Journal of Aerosol Science*, *8*, 149–159.
Tian, G., Hindle, M., & Longest, P. W. (2014). Targeted lung delivery of nasally administered aerosols. *Aerosol Science and Technology*, *48*, 434–449.
Tu, H., & Ray, A. K. (2005). Measurement of activity coefficients from unsteady state evaporation and growth of microdroplets. *Chemical Engineering Communications*, *192*, 474–498.
Wang, Y., & James, P. (1999). On the effect of anisotropy on the turbulent dispersion and deposition of small particles. *International Journal of Multiphase Flow*, *25*, 551–558.
Wu, D., Tawhai, M. H., Hoffman, E. A., & Lin, C.-L. (2014). A numerical study of heat and water vapor transfer in mdct-based human airway models. *Annals of Biomedical Engineering*, *42*, 2117–2131.
Xi, J., Kim, J., Si, X. A., & Zhou, Y. (2013). Hygroscopic aerosol deposition in the human upper respiratory tract under various thermo-humidity conditions. *Journal of Environmental Science and Health, Part A*, *48*, 1790–1805.
Yan, J., Yu, X., & Wang, Y. (2004). *Thermodynamic property tables and diagram for water and steam* (2nd ed.) Beijing: Higher Education Press.
Zhang, Z., Kleinstreuer, C., Kim, C. S., & Cheng, Y. S. (2004). Vaporizing microdroplet inhalation, transport, and deposition in a human upper airway model. *Aerosol Science and Technology*, *38*, 36–49.
Zhang, Y., Finlay, W., & Matida, E. (2004). Particle deposition measurements and numerical simulation in a highly idealized mouth–throat. *Journal of Aerosol Science*, *35*, 789–803.
Zhang, Z., Kleinstreuer, C., & Kim, C. S. (2006). Isotonic and hypertonic saline droplet deposition in a human upper airway model. *Journal of Aerosol Medicine*, *19*, 184–198.
Zhang, Z., Kim, C. S., & Kleinstreuer, C. (2006). Water vapor transport and its effects on the deposition of hygroscopic droplets in a human upper airway model. *Aerosol Science and Technology*, *40*, 1–16.
Zhang, Y., Chia, T. L., & Finlay, W. H. (2006). Experimental measurement and numerical study of particle deposition in highly idealized mouth-throat models. *Aerosol Science and Technology*, *40*, 361–372.
Zhang, Z., & Kleinstreuer, C. (2011). Laminar-to-turbulent fluid-nanoparticle dynamics simulations: Model comparisons and nanoparticle-deposition applications. *International Journal for Numerical Methods in Biomedical Engineering*, *27*, 1930–1950.
Zhang, Z., Kleinstreuer, C., & Hyun, S. (2012). Size-change and deposition of conventional and composite cigarette smoke particles during inhalation in a subject-specific airway model. *Journal of Aerosol Science*, *46*, 34–52.